Mechanical instability and percolation of deformable particles through porous networks

Eduard Benet, Guillaume Lostec, John Pellegrino, and Franck Vernerey[*]

Department of Mechanical Engineering, University of Colorado at Boulder, Boulder, Colorado 80309, USA

The transport of micron-sized particles such as bacteria, cells, or synthetic lipid vesicles through porous spaces is a process relevant to drug delivery, separation systems, or sensors, to cite a few examples. Often, the motion of these particles depends on their ability to squeeze through small constrictions, making their capacity to deform an important factor for their permeation. However, it is still unclear how the mechanical behavior of these particles affects collective transport through porous networks. To address this issue, we present a method to reconcile the pore-scale mechanics of the particles with the Darcy scale to understand the motion of a deformable particle through a porous network. We first show that particle transport is governed by a mechanical instability occurring at the pore scale, which leads to a binary permeation response on each pore. Then, using the principles of directed bond percolation, we are able to link this microscopic behavior to the probability of permeating through a random porous network. We show that this instability, together with network uniformity, are key to understanding the nonlinear permeation of particles at a given pressure gradient. The results are then summarized by a phase diagram that predicts three distinct permeation regimes based on particle properties and the randomness of the pore network.

I. INTRODUCTION

The transport and diffusion of soft, colloidal particles through porous media is at the heart of important processes in medicine [1,2] and biology [3] but also in areas such as cosmetics, food, or oil recovery [4]. These applications indeed rely on multiphase fluids that contain a myriad of small deformable particles (microbubbles, droplets, cells, bacteria, or viruses) that often need to permeate via physical barriers. For instance, the transport of bacteria through filtration membranes has shown a correlation between the permeation outcome and the size, shape, and deformability of the bacterial wall [5,6]. Particle deformability has also been found to be a major player in cell sorting using microfluidics [7], or in the permeation of nanoparticles through the openings in different organs such as the spleen [8]. However, while the differentiation of particles based on size [9], shape [10], or even pore characteristics [11,12] has been well studied, the role of their deformability is still poorly understood. The challenge in answering this question is the existence of two disparate length scales: the macroscale (or Darcy scale) and the microscale (or pore scale), both of which play distinct yet critical roles in particle transport. At the pore scale, models have been developed to elucidate the relation between particle mechanics [13–17] and motion [18–22] for different types of particles and flow conditions. Such relations typically characterize the entry of particles with various size, shape, structure, and adhesion properties [23–29] in narrow constrictions such as the nozzle of micropipettes. By contrast, Darcy scale models have concentrated on the effect of the porous medium (i.e., the pore network topology) on overall particle transport. In this context, Yiotis *et al.* have developed a lattice Boltzmann approach to study the coalescence and breakup dynamics of multiphase flows in porous media [30], while Foucard *et al.* used a finite-element approach [17,31] to study the effect of network geometry on soft particle transport [32]. The above models are usually computationally expensive and are thus limited to low particle numbers and small domains; this has precluded a more fundamental understanding of the problem at hand. Recognizing these limitations, alternative approaches based on statistical mechanics have been introduced to study transport in complex lattices [33,34]. The concept of percolation theory has proven to be critical in exploring a variety of situations involving the transport and spreading of multiphase fluids in porous media [35–39], the clogging mechanisms of rigid particles [40], or the spreading of micro-organisms in bioclogging [41] and bioremediation [42]. Despite this progress, there is not yet a theory that connects pore-scale models on soft particles to Darcy-scale models (involving network statistics).

The present work addresses this need by introducing a theoretical framework that can help us to understand and characterize the dynamics of a single particle traveling through a random medium under an overall pressure gradient. We focus in particular on situations in which the particles are larger than the average pore opening. In this case, particle deformability becomes an essential component of their transport by allowing them to squeeze through pore constrictions under sufficient pressure forces [15,43]. This mechanism has been used, for instance, for the construction of bubble-based logical circuits [44]. The objective of this study is to better understand how these concepts affect the nonlinear transport of droplets [45] in random networks. We also aim to characterize the role of droplet properties and network geometry in this process. This will be done in three steps. In the next section, we

---

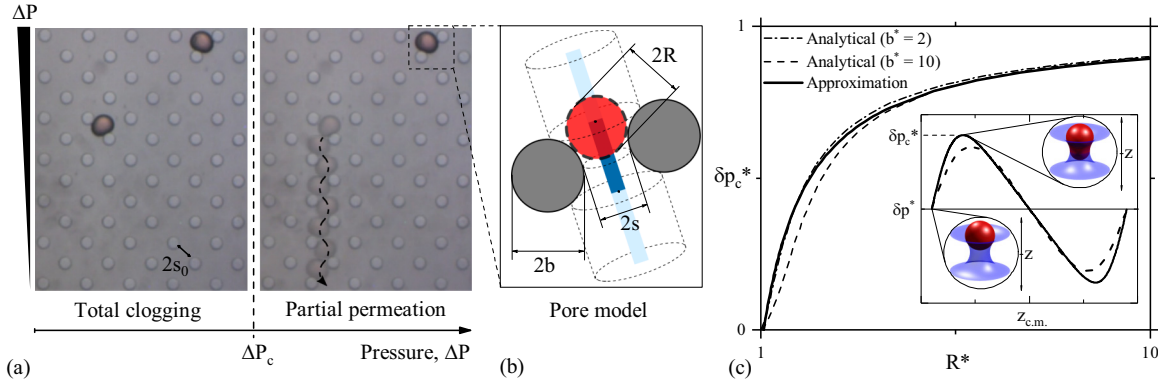[*]franck.vernerey@colorado.edu; https://www.colorado.edu/lab/vernerey/

FIG. 1. (a) Section of a PDMS microfluidic channel with a solution of hexadecane with two dispersed water droplets coated with SPAN-80. The system is subjected to an increasing pressure drop ΔP from top to bottom, which eventually (ΔP_c) pushes the smaller particle out of the system. (b) In the model of a porous medium, each pore is idealized as a connection of three axisymmetric sections in series whose direction is determined by the position of the obstacles. The external chambers are then assigned a permeability κ and the central one to a lower permeability κ_c that represents the narrowing of the pore throat. (c) The semianalytical solution [29] for the critical pressure ($\delta p_c^* = \frac{s}{2\gamma}\delta p_c$) vs the relative radius of the particle ($R^* = R/s$) is plotted for two toroidal pores ($b^* = 2, b^* = 10$). The results are compared to the approximation of Eq. (1) at $a = 1.068$ (solid line). The inset shows an example of a signature curve for a nonadhesive particle with radius $R^* = 1.5$ using a 3D approximation (solid line) [29] and a 2D one (dashed line) [43]. In it, the normalized equilibrium pressure drop (δp^*) is plotted against the position of the center of mass of the vesicle inside the pore ($z_{\text{c.m.}}$)

construct the transport model and highlight its connection to the mechanics of a soft particle permeating through a narrow pore. In Sec. III, the model is used in conjunction with percolation theory to predict particle transport in various conditions. In Sec. IV, we finally discuss the significance of these results and their connection to crowding and jamming in complex networks.

II. MODEL FORMULATION

We are interested here in characterizing the transport of deformable particles in a porous medium whose average pore size ($2s_0$) is smaller than the average particle diameter ($2R$). For the sake of simplicity, the particles are modeled here as immiscible fluid droplets with surface tension γ and no adhesion energy. However, the same analysis can be extended to particles with complex membranes or even elastic bodies. Such a situation was reproduced in the laboratory by fabricating a PDMS microfluidic channel in which we pushed a solution of hexadecane with dispersed water droplets coated with SPAN-80 [Fig. 1(a)]. In this experiment, the channel consists of an array of micropillars separated by a constant distance $2s_0$, and the solution was pushed using a global pressure drop ΔP. After successfully trapping droplets inside the channel, we made the following observations: for a small pressure drop, the droplets did not exhibit motion despite the surrounding fluid flow. However, as ΔP reached a critical value, the smaller droplet suddenly and rapidly permeated through the pillar network. The larger one eventually exhibited a similar behavior when subjected to a larger pressure. Although real porous networks are typically more random, these simple observations indicate that the permeation process is extremely fast compared to pore clogging, which implies that the permeation of soft colloids is a nonlinear process dominated by the latter. In other words, the model needs to be accurate regarding the critical pressure at which a particle permeates a pore, but it may remain approximate regarding the dynamics of a particle

between constrictions. Hence, we constructed a numerical model that considers the above system at two distinct scales: (a) at the pore scale, we will use an accurate solution to understand the critical pressure drop at which a particle is allowed to permeate. (b) At the Darcy scale, the porous network will be approximated as a network of long, cylindrical channels with a central constriction [Figs. 1(a) and 1(b)]where the flow will be resolved using the Hagen-Poiseuille solution. Our aim will be to quantify the effect of the porous medium geometry and topology on particle transport at both length scales.

Pore-scale physics have traditionally been investigated in the context of micropipette aspiration [46], microfluidics [47], and membrane filtration [48], among others. These studies showed that a deformable particle would remain trapped by a constriction unless the pore pressure (δp), i.e., the pressure difference across the pore, exceeded a critical pressure (δp_c) [15]. For pressures below the threshold ($\delta p \leqslant \delta p_c$), the particles block the pore but do not permeate. For pressures above the threshold ($\delta p > \delta p_c$), the particle becomes unstable and crosses the pore. We have recently characterized this behavior via a pressure-displacement curve shown in the inset of Fig. 1(c), which allows a evaluation of the critical pressure in terms of its size, surface tension, adhesion, and pore geometry [29]. We noticed that normalized solutions for different pore shapes, or even two-dimensional (2D) versus (3D) models [see the inset in Fig. 1(c)], follow the same trends. Hence, for the sake of clarity, we concentrate here on toroidal, axisymmetric pores [Fig. 1(c)] with internal constriction $2s$. In this scenario, δp_c scales linearly with the factor $2\gamma/s$ and its value varies with the relative size of the particles ($R^* = R/s$), and to a lesser extent, with the size of the pore ($b^* = b/s$). We found that a good estimation of the relationship between the critical pressure and the normalized particle radius is provided by

$$\delta p_c = \begin{cases} 0 & \text{if} \quad R^* \leqslant a, \\ \frac{2\gamma}{s}\left(1 - \frac{a}{R^*}\right) & \text{if} \quad R^* > a, \end{cases} \quad (1)$$
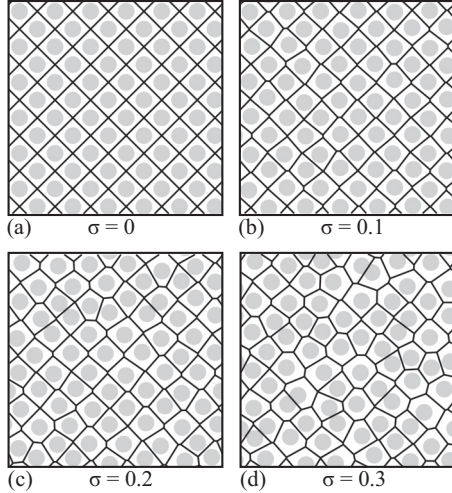
FIG. 2. Example of four networks at different values of the randomness parameter $\sigma = 0$, 0.1, 0.2, and 0.4. The networks are created in a domain $L_x = L_y = [-1, 1]$ for an average value $s_0 = 0.08$ and $b/s_0 = 2$. The lines represent all the pores in the system regardless of their pressure or open or closed state.

where a is a constant depending on the pore shape and size (b). In the rest of this article, we considered toroidal pores with $b^* = 2$, for which we obtained $a = 1.068$.

Let us now explore how this pore-scale response affects the transport of particles at the Darcy scale. For this, we first need to characterize the pressure distribution and fluid flow in a porous medium modeled as a network of constricted pipes [49,50]. A single pore is regarded here as the connection of three axisymmetric sections connected in series: two wider chambers with a permeability κ, and a central, narrower one with a permeability κ_c representing the pore throat. For throat diameters on the order of microns, flows are in the Stokes regime so that the fluid flux q in a section can be determined as $q = -\kappa[p]$, where $[p]$ is the pressure difference across the chamber. Using the Hagen-Poiseuille solution, the permeability can further be found as $\kappa = \frac{\pi r^4}{8\mu L}$, where r corresponds to the radius of the section, μ is the viscosity of the fluid, and L is the length of the chamber. Note that these assumptions would break down for larger Reynolds numbers (i.e., larger pores or small viscosities).

Such a network of pipes was constructed in a rectangular, two-dimensional domain $\Omega = 2L_x \times 2L_y$, where pores are generated with a periodic Voronoi diagram based on the center of randomly located circular obstacles (Fig. 2). The channel constrictions are then determined based on the space between obstacles. Hence, the network geometry is characterized by three main parameters: (i) the size b of the obstacles, (ii) the average distance $2s_0$ between them, and (iii) the randomness σ of their location (see Appendix A for details on obstacle collocation). As shown in Fig. 2, σ is a measure of the disturbance of the obstacle location from that of a perfect lattice arrangement. We found that as long as $\sigma \leqslant 0.3$, the obstacles do not excessively overlap, and the pore size follows a truncated normal distribution $f_s \sim N(s, \sigma)$. This is consistent with the fact that most porous networks are characterized by the distributions of their pores throats f_s, which are commonly taken as log-normal

or truncated normal distributions [51]. We therefore limit ourselves to this range for the remainder of the paper. The network is then solved considering the pressure at each node in the vector $\boldsymbol{p}$, and determining its value by enforcing the local balance of mass on each node ($\sum q = 0$). This leads to the linear system $\boldsymbol{K}\boldsymbol{p} = \boldsymbol{0}$, where $\boldsymbol{K}$ is the node conductance matrix [52]. To account for the fact that we are only modeling a portion of a larger porous media, we solved the system using periodic boundary conditions enforcing equal flux on each boundary ($q_{\text{left}} = q_{\text{right}}$ and $q_{\text{top}} = q_{\text{bottom}}$) and a vertical pressure drop ΔP ($p_{\text{left}} = p_{\text{right}}$ and $p_{\text{bottom}} = p_{\text{top}} + \Delta P$).

Let us now consider the motion of a single particle within this network. In this context, we recognize that the particle's effect is twofold: (a) if the particle is in a constriction whose pressure drop $[p]$ is below its critical value, it remains immobile, and the pore permeability is significantly reduced. In this study, we assume that the permeability vanishes ($\kappa_c = 0$). Hence, the trapped particle divides the pore into two chambers of constant pressure and zero flux whose values are determined by solving the previous linear system. (b) If the local pressure drop $[p]$ exceeds its critical value, the particle will cross the pore. In other words, there is a two-way coupling between fluid and particle transport. When the particle is trapped, it blocks a single pore and locally redistributes flow and pressures. This redistribution may feed back onto the particle and either accelerate or postpone its permeation depending on the local network topology. Hence, we will define the pore pressure (δp) on channel i as the pressure drop $[p]$ obtained by solving the linear system with $\kappa_c^i = 0$. This corresponds to the effective pressure applied to a trapped particle.

Finally, let us introduce the following normalization on the pressure gradient: $\nabla P^* = \nabla P(L_y^2/\gamma)$, which will allow us to concentrate on the effects of particle size (R^*) and network uniformity (σ). Using this normalization, we further performed a convergence analysis to determine the optimal network size to avoid boundary effects. We observed that for a square domain and parameter $s_0^* = s_0/L_y \leqslant 0.015$, the distributions for both the pore size and nodal pressures converged with an error below 1%, so we will stay in this range for the remainder of the paper.

III. NETWORK PERMEABILITY AND PERCOLATION THEORY

To determine whether a particle can percolate through the pore network, one needs first to estimate its chances of passing through a series of constrictions whose pressure drop δp is larger than the critical value δp_c. For this, let us split the pore population into three categories (Fig. 3): (i) wide pores (with a number fraction O_w) are characterized by a throat size that is larger than the particle (i.e., $\delta p_c = 0$); (ii) narrow pores (with a number fraction O_n), whose size is smaller than the particles ($\delta p_c > 0$); and (iii) blocked pores (with a number fraction O_b) that can never be crossed because the obstacles are touching or overlapping ($s < 0$). This information can be found via the knowledge of the pore throat distribution f_s as

$$O_w = 1 - P(s \leqslant R) \quad \text{and} \quad O_b = P(s \leqslant 0), \qquad (2)$$

where P is the cumulative distribution of f_s. Because these pores span the entire pore population, the number fractions
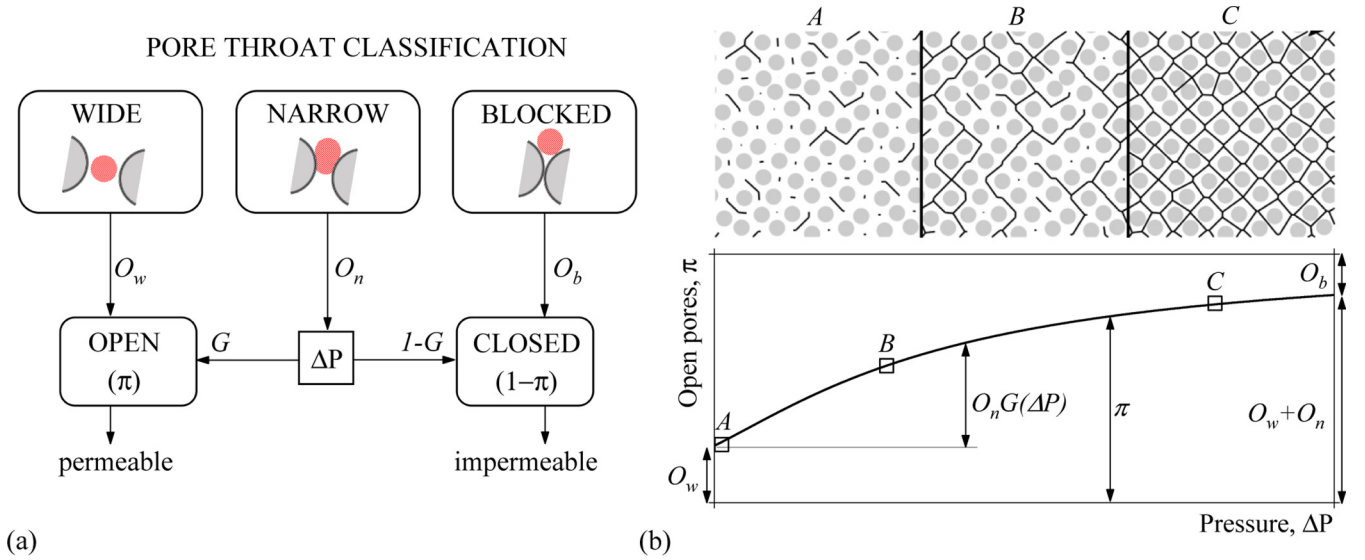
FIG. 3. (a) Scheme of the pore classification according to their geometry [wide (O_c), narrow (O_n), and blocked (O_b)] and their status [opened (π) or closed ($1 - \pi$)]. These two classifications are related via the pressure drop ΔP, which determines the proportion of narrow, open pores G. (b) Evolution of the probability π as a function of the pressure. The three insets show a pore network at different pressure drops in which the channels where $\delta p > \delta p_c$ (regardless of their connectivity) are depicted with black lines.

satisfy the condition $O_w + O_n + O_b = 1$. To relate these fractions to particle transport, we further subdivide the population of narrow pores by their open (particles permeate through them) and closed (particles do not permeate through them) fractions G and $1 - G$, respectively. It is clear here that the fraction $G = G(\Delta P)$ is dependent on pressure gradient, i.e., for low pressure gradient $G \to 0$, while when the pressure is large, all pores are open and $G \to 1$. Based on this classification, the total fraction of open (π) and closed ($1 - \pi$) pores is written, respectively, as

$$\pi = O_w + O_n G, \tag{3a}$$

$$1 - \pi = O_b + (1 - G)O_n. \tag{3b}$$

Note that both G and π are monotonically increasing functions of the pressure. Indeed, for pressures close to zero ($G \to 0$), the particle can only permeate through those spaces that require no deformation, $\pi = O_w$. As this pressure increases, more constrictions become permeable (not necessarily connected) until the total amount of open pores reaches its maximum at $\pi = 1 - O_b$ (Fig. 3).

Interestingly, once the proportion (π) of open pores is known, it is possible to estimate particle permeation through the porous medium by determining the probability θ of finding an open path that connects both ends of the network. This quantity might be estimated with directed bond percolation via the power law

$$\theta(\nabla P) \begin{cases} 0 & \text{if } \pi < \pi_c, \\ \sim [\pi(\nabla P) - \pi_c]^\beta & \text{if } \pi > \pi_c, \end{cases} \tag{4}$$

where π_c and β are constants that only depend on network topology and dimension. On the one hand, the exponent β is a universal constant that only varies with the spatial dimension of the problem [53]. For the two-dimensional lattices considered in this article, this value is estimated at $\beta = 0.277$ [54]. On the other hand, π_c corresponds to the percolation threshold that

separates an absorbing (i.e., no particles permeating) from a percolating state. This value is also completely independent of the physics discussed here and depends only on the dimension of the problem and the pore lattice [55].

From (3) and (4), it is clear that our understanding of particle permeation eventually relies on finding the probability function $G(\Delta P)$, interpreted here as the likelihood that $\delta p > \delta p_c$ for any pore in the network. To this end, if we introduce the probability distribution $f_\cap$ of finding a pore with given values of δp and δp_c, the fraction G is then found as the integral

$$G = \int_0^\infty \left(\int_{\delta p_c}^\infty f_\cap(\delta p_c, \delta p) d(\delta p) \right) d(\delta p_c). \tag{5}$$

To determine the distribution $f_\cap$, we note that the calculation of the pore pressure (δp) does not depend on the pore-particle properties, i.e., it is only a function of the network topology. In contrast, the critical permeation pressure (δp_c) is exclusively a function of the pore-scale characteristics (size and shape of the pore) and does not depend on the pore location within the network. As a consequence, the variables δp_c and δp can be treated as independent, and the probability density $f_\cap$ becomes the product of two simple probability functions:

$$f_\cap = f_c f_p, \tag{6}$$

where f_c and f_p denote, respectively, the probability density function of δp_c and δp in narrow pores. Let us next determine their expressions in terms of network and particle properties.

A. Probability density function of the critical pressure (δp_c)

Since the probability distribution f_s of the pore throats is known from the network geometry, it is possible to find the distribution of any continuous and differentiable function that depends on f_s. In particular, using the relation $\delta p_c = \delta p_c(s)$ established in Eq. (1), we can write the actual
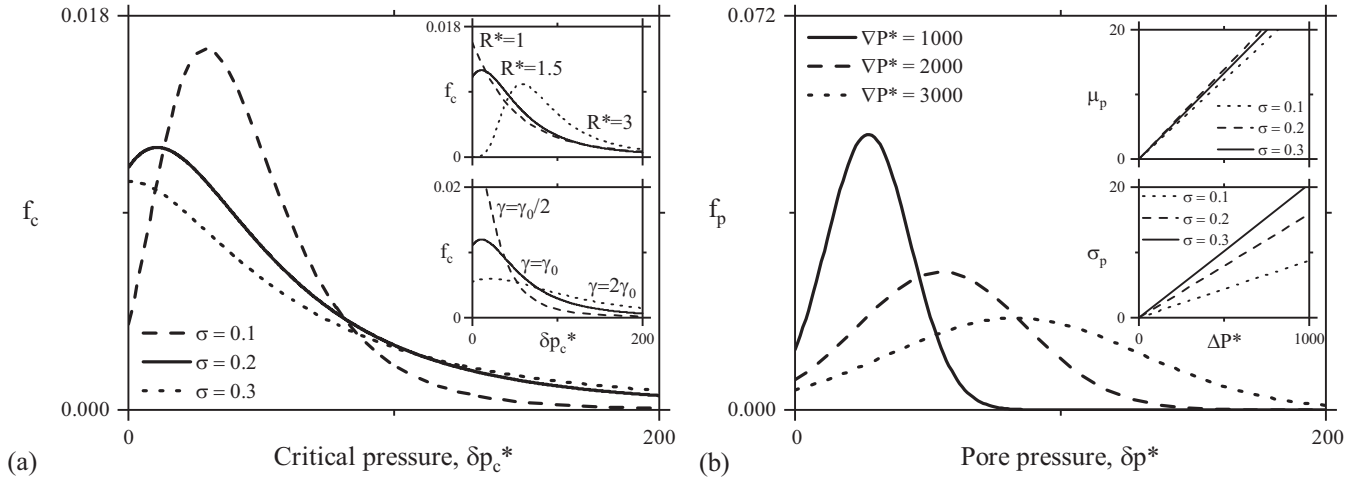
FIG. 4. (a) Density distribution of the critical pressure on three different networks with $\sigma = 0.1$, 0.2, and 0.3. The top inset shows the same curves for three different values of the relative radius R^*, and the bottom one is the same problem but for three different values of the surface tension, where we took $\gamma_0 = 1$. (b) Density distribution of the pore pressure for three different values of the relative pressure gradient applied to the system. The two insets show the evolution of the mean and standard deviation of the pore pressure in three different networks ($\sigma = 0.1 - 0.3$).

density distribution of the critical pressure in narrow pores as (Appendix B)

$$f_c = \frac{s^2}{2\gamma} \frac{f_s}{O_n}, \qquad (7)$$

where $s(\delta p_c)$ is found by inverting Eq. (1). Figure 4(a) shows the distribution of the critical pressure on three networks characterized by different values of sigma ($\sigma = 0.1$, 0.2, and 0.3). As expected, in uniform networks (small σ), the distribution is concentrated around the average value $\delta p_c(s_0)$. This distribution, however, tends to spread out as the network loses regularity. We also note that the peak of the distribution shifts to lower pressure values, which is a consequence of finding more wide pores in the network. The effects of surface tension and the relative radius of the particles are further shown in the insets of Fig. 4. We see there that those two parameters exhibit similar trends: a lower surface tension γ or small particle size R^* improve particle permeation by lowering their critical pressure δp_c.

B. Probability density function of the pore pressure (δp)

This distribution was found by fitting the results given by numerical simulations. More specifically, for a given macroscopic pressure drop, the value of δp on each pore was determined by setting its permeability to zero to simulate a blocked particle in the pore. This process was then repeated on a large number of network models following the same statistics until the histograms converged with an error below 1%. The results showed that for values of $\sigma < 0.3$, the pore pressure in narrow pores is well approximated by a normal distribution as

$$f_p \sim N(\mu_p; \sigma_p), \qquad (8)$$

where μ_p and σ_p are, respectively, the mean and standard deviation. Appendix C shows the details of the calculation as well as the obtained values of μ_p and σ_p for each value of σ. Additionally, since the solution comes from a linear

system, this distribution will also scale linearly with the applied pressure, i.e., $\mu_p = \nabla P^* \mu_p^1$ and $\sigma_p = \nabla P^* \sigma_p^1$, where μ_p^1 and σ_p^1 correspond to the solution at $\nabla P^* = 1$. As a result, the
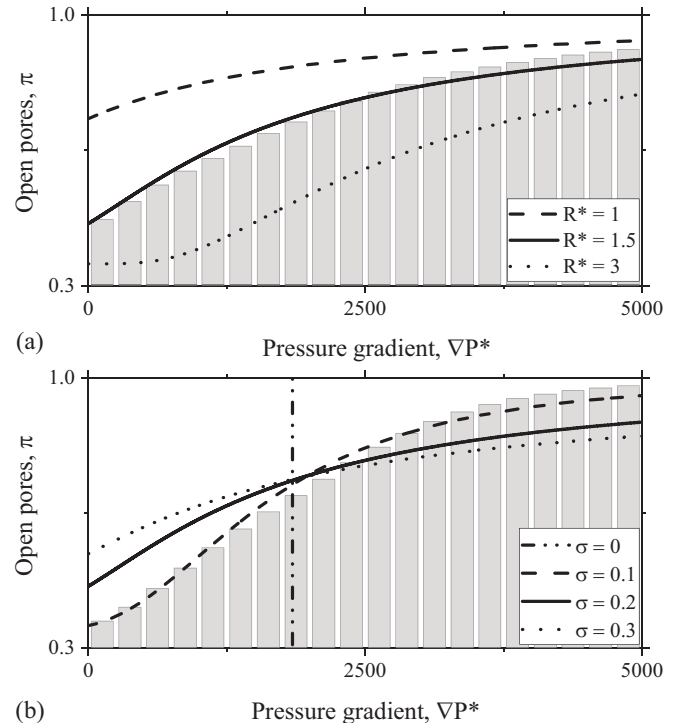

FIG. 5. Evolution of the probability π with the applied pressure on the system. (a) The probability is plotted for three different particles with radii $R^* = 1$, 1.5, and 3 and a network with parameter $\sigma = 0.2$. (b) The same curves are plotted here for four different networks with values of $\sigma = 0$, 0.1, 0.2, 0.3, and a radius $R^* = 1.5$. The vertical bars in both graphics correspond to the numerical histograms of the network for two different values of $\sigma = 0.1$ and 0.2 and a particle of radius $R^* = 1.5$.
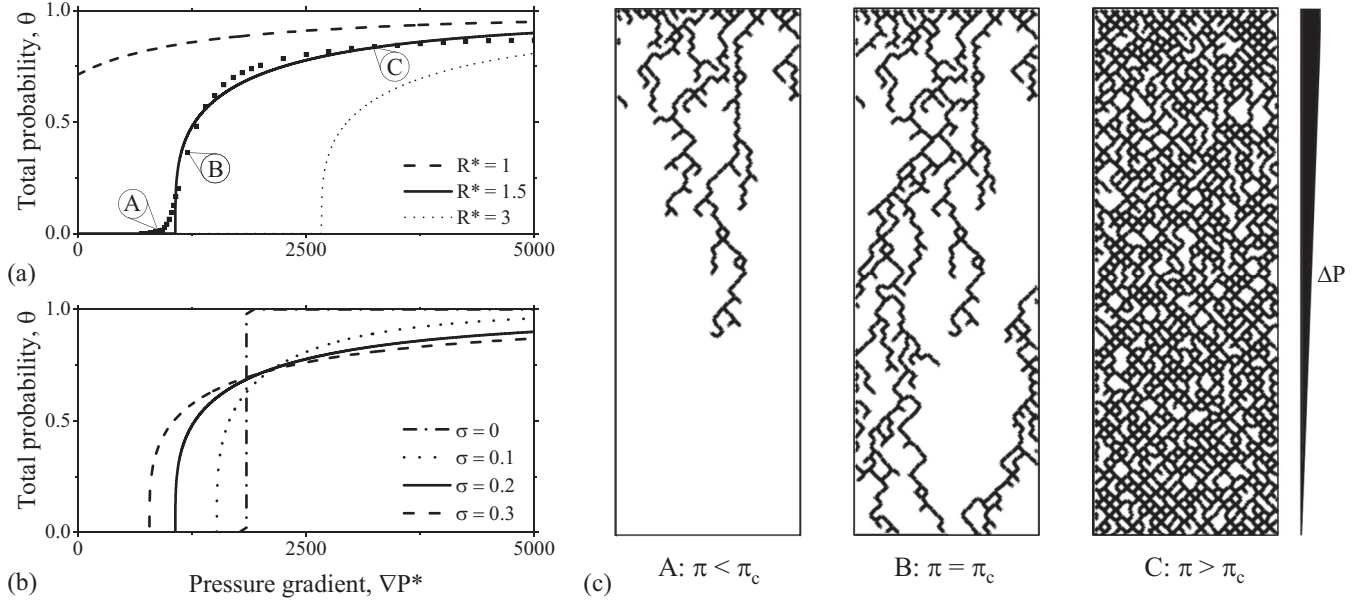
FIG. 6. The probability of generating an infinite cluster θ vs the normalized pressure gradient applied to the system. (a) The top graphic shows the probability on a network with $\sigma = 0.2$ and three different particles with radius $R^* = 1$, 1.5, and 3. The dots compare the results with the obtained results from numerical simulations. Part (b) shows the same evolution for a particle with $R^* = 1.5$ and three different networks with $\sigma = 0$, 0.1, 0.2, and 0.3. (c) The insets A, B, and C show three examples of the obtained percolation network at $\pi < \pi_c$, $\pi = \pi_c$, and $\pi > \pi_c$.

function f_p translates to higher values and spreads out as the macroscopic pressure gradient ∇P increases [Fig. 4(b)]. We further found that while the mean pore pressure μ_p is not very sensitive to network uniformity σ [insets in Fig. 4(b)], the standard deviation σ_p does increase with σ.

By introducing expressions (7) and (8) into (3a) and (5), it is now possible to express how the proportion of open pores (π) grows with applied pressure drop ΔP. Furthermore, it is possible to understand the effect of geometrical parameters such as pore shape, particle size, and surface tension via the functions f_c and f_p. However, since there is no simple analytical solution for the integral in (5) and the obtained distributions, we used numerical integration (Appendix D) to obtain the results shown in Fig. 5 for different scenarios. These results were further verified by computing the actual value of π from direct numerical simulations where π was determined as the average number of open pores ($\delta p_c > \delta p$) divided by the total number of pores. The results plotted in Fig. 5 correspond to a total number of networks such that the histograms converged with an error below 1%. We observe an excellent agreement between the numerical results and our predictions, with a maximum relative error of 1.2% between the analytical and numerical predictions. The results show how the amount of open pores at zero pressure (O_w) decreases with particle size and network uniformity (low σ). A similar observation can be made for blocked pores (O_b) as we are less likely to find them in regular networks or for large particles. We further see that the proportion of open pores increases nonlinearly with the pressure gradient with a steeper increase around $\delta p_c(s_0)$ [Fig. 5(b)], the pressure at which approximately half the narrow pores open. As the network becomes more regular, both the distributions δp_c and δp become more uniform and the transition between closed and open pores occurs at a

narrower region of the applied pressure. As expected, when $\sigma = 0$, the distribution becomes a perfect step function.

To close this section, we need to determine the value of π_c. For this, we defined θ as the fraction of top nodes connected (via open pores) to the bottom edge at a given pressure. Its value was then determined by simulating several random scenarios until the values converged. We noticed that a minimum domain of $L_y = 3L_x$ was needed to avoid boundary effects in the computation of θ; see Fig. 6(a). Knowing the functions of $\pi(\Delta P)$ and $\theta(\Delta P)$, we can construct the percolation curve ($\theta - \pi$) and determine π_c by fitting $\theta = (\pi - \pi_c)^{0.277}$. We found that π_c varies nonlinearly from 0.64 to approximately 0.6 when $\sigma = 0.3$, which is consistent with values reported in the literature ($\pi_c = 0.6447$) for square lattices in a diagonal direction [56].

IV. RESULTS AND DISCUSSION

We are now in a position to explore how the probability θ relates to the overall permeability of particles through the network. In Fig. 6 we plot the evolution of this probability as a function of the applied pressure and for different variations of the particle size and network randomness. Two main observations can be drawn from these results.

(i) There is a critical pressure ∇P_c analogous to π_c below which there is no droplet permeation. This pressure increases with the particle size and network uniformity. The effect of droplet size is expected since larger particles typically require more pressure to permeate the same pore [Fig. 1(c)]. The effect of network uniformity is, however, less intuitive and may be interpreted by the fact that nonuniform networks (larger σ) have a larger chance of creating a wider path (with lower ∇P_c). These networks also possess a larger number of
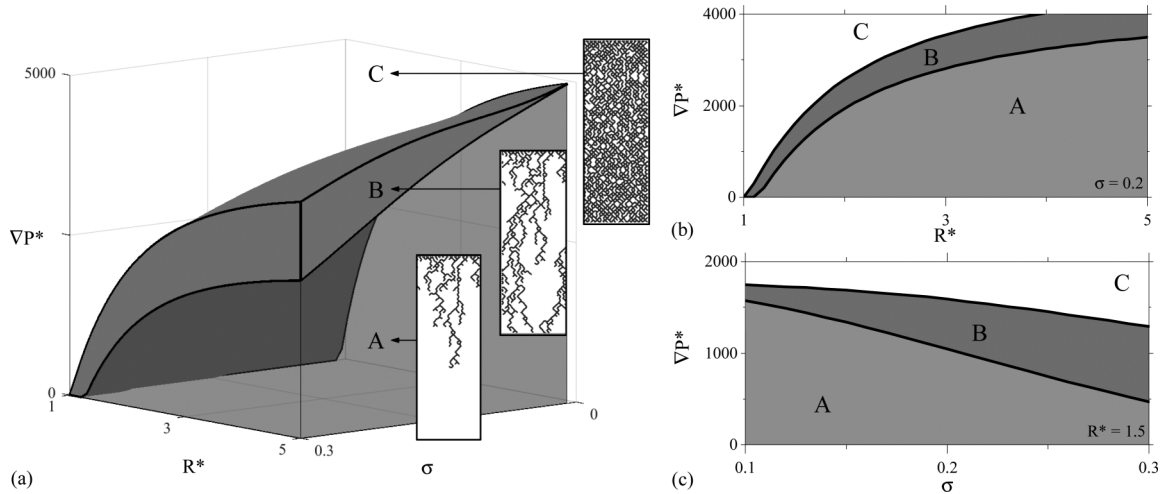
FIG. 7. (a) Phase diagram of the three different permeating stages of the porous network as a function of the relative particle radius R^*, network uniformity σ, and applied pressure ∇P^*. Slices of the phase diagram at the values of $\sigma = 0.2$ (b) and $R^* = 1.5$ (c) showing the variation of the minimum pressure (or ∇P_c^*) and the semipermeable or permeable distinction.

narrower throats; this means that a higher pressure is required to converge to $\theta = 1 - O_b$. Furthermore, the numerical curves exhibit a small tail around ΔP_c, which induces imprecisions in the numerical evaluation of ΔP_c. This is a consequence of the finite size of our system, and it is known to disappear as the domain becomes infinite [57,58].

(ii) The behavior predicted by these curves is divided into three stages. The network is (a) droplet-impermeable below ∇P_c, i.e., only the fluid is able to permeate. Once this value is reached, there is a sharp increment around ($\nabla P = \nabla P_c$) where the network undergoes a (b) weakly permeable transition as θ increases rapidly. In this regime, the number of available paths reduces as the droplet moves through the network [Fig. 6(c)]. Finally, the network becomes strongly permeable (c) when the majority of pores are open. In this regime, the probability θ keeps increasing with pressure, but this occurs at a much lower rate. The size of the clusters exhibited in each of these three regions is also given by universal exponents and the critical pressure. Hence, given the probability p, their values are only a function of each lattice type [53].

Interestingly, when the applied pressure is relatively low, the trajectory taken by the droplet eventually tends to converge to a single path [regime A and B, Fig. 6(c)]. To understand this, we first note that the trajectory chosen by a droplet at a junction between pores [59,60] is driven by the direction of maximum fluid velocity. Consequently, particles tend to be attracted to series of connected pores in which the fluid velocity is maximum, which is analogous to the enhanced fluid flux when a crack is present in fractured porous media [61,62]. This implies that soft particles in a dilute system are inevitably attracted and concentrate in a specific region within the network, while other regions remain totally unexplored. This effect, however, disappears for larger pressures since particles are allowed to permeate more pores.

To better understand the distinct roles of particles and network on permeation, we show in Fig. 7(a) a phase diagram showing the three regions (A, B, and C) in the parameter space (R^*, σ). In this diagram, the boundary between regions A and B is given by the condition $\nabla P = \nabla P_c$, while the

boundary between B and C is chosen as the value of ∇P when 50% of narrow pores are open (corresponding to a global probability $\theta \approx 0.7$). The diagram shows that the weakly permeable regime (B) only exists as the network becomes nonuniform. Indeed, highly uniform networks tend to have an "all or nothing" response in which all pores open at the same critical pressure, Fig. 6(b). This response smoothes out as lattice disorder is introduced. A similar effect is observed as the relative size of the particle is varied; smaller particles tend to percolate at a smaller range of pressures reducing the range of the weakly permeable regime.

V. CONCLUSIONS

In summary, we presented a theoretical framework based on directed percolation in order to describe the permeation of soft particles in random pore networks. Focusing on a dilute concentration of particles whose size is comparable to that of the pores, we found that permeation is a highly nonlinear function of applied pressure. The model predicts the existence of three regimes of permeation: (a) when the applied pressure is smaller than a critical value, particles are unable to permeate the pores and remain jammed in the network. (b) When the applied pressure exceeds this critical value, the system enters a so-called weakly permeable regime, during which particles tend to converge to predefined trajectories and thus only explore limited regions of the network. (c) When the applied pressure is large, particles are able to permeate through most of the pores in the network, and a strongly permeable regime is observed. Importantly, our model shows how these behaviors vary in terms of particle size, properties, and network geometry. A phase diagram was constructed to visualize the effect of these physical parameters on the system's response. This may provide a useful tool with which one can tune the operational pressure ΔP applied on a membrane or microfluidic device in order to meet a particular objective such as permeation, separation, or trapping.

On a final note, while this work concentrated on simple droplets (characterized by their size and surface tension) and

pore shapes (toroidal), it is possible to include other important physics related to varying pore shape, size, or even pore-droplet adhesion. This can be done by modifying the critical pressure defined in Eq. (1) based on previous studies [29]. Furthermore, the role of particle kinetics was not explored, but we expect it to play a large role in subsequent jamming at higher concentrations. Future models may, therefore, include the time necessary to permeate a pore, which can be determined via time-dependent pore-scale models of particle permeation [15,20,22]. Viscoelastic models of particle deformation should also be considered in the future [63]. We further expect the system's behavior to deviate from our predictions when the droplet concentration increases above the dilute regime. In this situation, the presence of multiple droplets will tend to drastically change the pressure distribution on the network and probably lower the critical pressure for permeation as predicted in a previous study [43]. Further research effort will, therefore, be necessary to fundamentally understand the motion of soft particles or macromolecules in porous media under the action of driving pressure, self-propulsion [64], and more. Applications in particle separation, filtration, sorting, as well as our ability to control macromolecule transport in polymers for tissue engineering [65–67] will depend critically on this understanding.

APPENDIX A: NETWORK CONSTRUCTION

We describe here the general approach taken to construct a random network of pores inside a square domain $2L_x \times 2L_y$. We start by locating a diamond grid of equally spaced, circular obstacles of radius b, where the space left between two obstacles is $2s_0$; see case $\sigma = 0$ in Fig. 2. The randomness is then introduced by moving the center of each obstacle ($\boldsymbol{x}_i$) a random distance and direction $\boldsymbol{dx} = [dx, dy]$, where dx and dy are taken from a random normal distribution $N(0, \sigma_s)$. For convenience, we took $\sigma_s = 2s_0\sigma$, where σ is a parameter that allows us to control the level of randomness in the system. The final position of the pores is obtained by generating a Voronoi diagram based on the resulting location of the obstacles' center. The throat size of each pore is then assigned as the minimum distance between the edges of the circles. This method, however, introduces a lot of small-sized pores that simply connect different nodes at the junctions but which have no constriction; they are part O_w. Hence, we only use the word "pores" to refer to those connections in the system whose length is at least as long as the obstacle ($2b$). Using these rules, we observed that the resulting pore throats follow a normal distribution such that

$$s \sim N(s_0, \sigma s_0), \tag{A1}$$

where s_0 and σs_0 are the mean and standard deviation, respectively.

APPENDIX B: CRITICAL PRESSURE DISTRIBUTION

The critical pressure is a magnitude that can only be defined in narrow pores ($0 < s < R$). Additionally, we know from Eq. (1) that δp_c is related to s by the following expression:

$$s = \frac{2\gamma R}{\delta p_c R + 2\gamma a}, \tag{B1}$$

so we can redefine the distribution of δp_c as a conditional probability density function $f_c = f_c(\delta p_c | 0 < s < R)$, i.e., the probability density of δp_c constrained to the narrow pores. Since the distribution of pore throats f_s is known, we can use Eq. (B1) to derive the distribution of f_c. For this, we start by building the cumulative distribution of the critical pressure (P_c) and write

$$P_c = 1 - P(\delta p_c > X | 0 < s < R), \tag{B2}$$

where X is any given value of δp_c. Using the Bayes theorem, we can rewrite this function as

$$P_c = 1 - \frac{P(0 < s < R | \delta p_c > X) P(\delta p_c > X)}{P(0 < s < R)}, \tag{B3}$$

where the probability $P(0 < s < R | \delta p_c > X)$ is equal to 1 since constrictions with nonzero critical pressure will naturally be narrow pores. The bottom probability $P(0 < s < R)$ simply corresponds to the fraction of narrow pores, or O_n. Hence, we can rewrite the value of P_c as

$$P_c = 1 - \frac{P(\delta p_c > X)}{O_n}. \tag{B4}$$

From Eq. (B1) we can directly establish that the probability $P(\delta p_c > X)$ is equivalent to $P[0 < s < s(X)]$, which is found using the cumulative density distribution of the pore size. Based on that, we can write

$$P_c = 1 - \frac{P[s < s(X)] - O_b}{O_n}. \tag{B5}$$

Finally, the probability density can be found by taking the derivative as

$$\begin{aligned} f_c &= \frac{\partial P_c}{\partial (\delta p_c)} = -\frac{f_s}{O_n} \frac{\partial s}{\partial (\delta p_c)} \\ &= \frac{2\gamma R^2}{(\delta p_c R + 2\gamma a)} \frac{f_s}{O_n} = \frac{s^2}{2\gamma} \frac{f_s}{O_n}, \end{aligned}$$

which implies that the distribution of the critical pressure given a particle size can be directly found from the distribution of pore throats.

APPENDIX C: PORE PRESSURE DISTRIBUTION

Our simulations showed that the distribution of the pore pressure was strongly correlated with the pore throat distribution. To determine this relationship in a single network, we first computed the pore pressure (δp) for each channel at a pressure gradient $\Delta P^* = 1$. Then, we constructed the corresponding frequency histogram based on the obtained results. This process was repeated for a large number of networks until the average of the histograms converged with an error below 1%. We observed that for the range $0 < \sigma < 0.3$, the normalized histogram of the pore pressure is well approximated by a

truncated normal distribution. The parameters of this normal were found next using least-squares fitting. The following table summarizes the obtained values for a normalized network with $s^* = 0.015$, $b^* = 0.015$, and $L_y = 3L_x$:

σ	μ_p^1	σ_p^1
0	0.0208	0
0.1	0.0245	0.0087
0.2	0.0276	0.0159
0.3	0.0265	0.0205

APPENDIX D: PROBABILITY OF CROSSING A NARROW PORE (G)

The probability of crossing a single pore depends on the probability distribution of both the critical pressure and the pore pressure. Hence, this result might vary among problems. In this work, we obtained two normal distributions, which can be introduced here to obtain

$$G = \int_0^\infty \frac{s^2 e^{-\frac{(\bar{s}-s)^2}{2\sigma_s^2}}}{2\gamma\, O_n \sqrt{2\pi}\,\sigma_s} \left(\int_{\delta p_c}^\infty \frac{e^{-\frac{(\delta p - \delta p)^2}{2\sigma_p^2}}}{\sqrt{2\pi}\,\sigma_p} d(\delta p) \right) d(\delta p_c). \quad (D1)$$

Since our system is originally defined based on the distribution of pore sizes, we can integrate the second part and introduce

a change of variable as defined in Eq. (B1). Hence, we obtain an integral on the pore distribution as

$$G = \frac{\int_0^{R/a} \left[1 - \mathrm{erf}\left(\frac{\delta p_c(s) - \delta p}{\sigma_p \sqrt{2}} \right) \right] e^{-\frac{(\bar{s}-s)^2}{2\sigma_s^2}} ds}{O_n \sqrt{2\pi}\,\sigma_s}. \quad (D2)$$

This equation can be further simplified to obtain the following expression:

$$G = A - B \int_0^{R/a} \mathrm{erf}\left(\frac{C}{s} - D \right) e^{-\frac{(\bar{s}-s)^2}{2\sigma^2}} ds, \quad (D3)$$

where

$$A = -\frac{1}{4O_n} \mathrm{erf}\left(\frac{R/a + \bar{s}}{\sqrt{2}\sigma} \right),$$

$$B = \frac{1}{2O_n \sqrt{2\pi\sigma^2}},$$

$$C = \frac{2\gamma}{\sqrt{2}\sigma_p},$$

$$D = -\frac{2}{\gamma a} R \sqrt{2}\sigma_p - \frac{\mu_p}{\sigma_p},$$

which was integrated numerically.

[1] A. Drochon, D. Barthes-Biesel, C. Bucherer, C. Lacombe, and J. C. Lelievre, Biorheology **30**, 1 (1993).

[2] C. E. Ashley, E. C. Carnes, G. K. Phillips, D. Padilla, P. N. Durfee, P. A. Brown, T. N. Hanna, J. Liu, B. Phillips, M. B. Carter, N. J. Carroll, X. Jiang, D. R. Dunphy, C. L. Willman, D. N. Petsev, D. G. Evans, A. N. Parikh, B. Chackerian, W. Wharton, D. S. Peabody, and C. J. Brinker, Nat. Mater. **10**, 476 (2011).

[3] M. W. Stefferson, S. A. Norris, F. J. Vernerey, M. D. Betterton, and L. E. Hough, Phys. Biol. **14**, 045008 (2017).

[4] R. W. Baker, *Membrane Technology and Applications* (Wiley, Chichester, UK, 2012).

[5] N. Lebleu, C. Roques, P. Aimar, and C. Causserand, J. Membr. Sci. **326**, 178 (2009).

[6] A. Gaveau, C. Coetsier, C. Roques, P. Bacchin, E. Dague, and C. Causserand, J. Membr. Sci. **523**, 446 (2017).

[7] P. Preira, V. Grandné, J.-M. Forel, S. Gabriele, M. Camara, and O. Theodoly, Lab Chip **13**, 161 (2013).

[8] R. A. Petros and J. M. DeSimone, Nat. Rev. Drug Disc. **9**, 615 (2010).

[9] G. Hvichia, Z. Parveen, C. Wagner, M. Janning, J. Quidde, A. Stein, V. Müller, S. Loges, R. Neves, N. Stoecklein, H. Wikman, S. Riethdorf, K. Pantel, and T. Gorges, Int. J. Cancer **138**, 2894 (2016).

[10] Y. Wang, F. Hammes, M. Düggelin, and T. Egli, Environ. Sci. Technol. **42**, 6749 (2008).

[11] S. M. McFaul, B. K. Lin, and H. Ma, Lab Chip **12**, 2369 (2012).

[12] A. F. Sarioglu, N. Aceto, N. Kojic, M. C. Donaldson, M. Zeinali, B. Hamza, A. Engstrom, H. Zhu, T. K. Sundaresan, D. T. Miyamoto, X. Luo, A. Bardia, B. S. Wittner, S. Ramaswamy, T. Shioda, D. T. Ting, S. L. Stott, R. Kapur, S. Maheswaran, D. A. Haber, and M. Toner, Nat. Methods **12**, 685 (2015).

[13] F. J. Vernerey and M. Farsad, Comput. Methods Biomech. Biomed. Eng. **14**, 433 (2011).

[14] L. Foucard, X. Espinet, E. Benet, and F. J. Vernerey, in *Multiscale Simulations and Mechanics of Biological Materials* (John Wiley & Sons, Ltd., 2013), pp. 241–265.

[15] R. Kusters, T. Van Der Heijden, B. Kaoui, J. Harting, and C. Storm, Phys. Rev. E **90**, 033006 (2014).

[16] L. Foucard, A. Aryal, R. Duddu, and F. Vernerey, Comput. Methods Appl. Mech. Eng. **283**, 280 (2015).

[17] L. C. Foucard and F. J. Vernerey, Int. J. Numer. Methods Eng. **107**, 923 (2016).

[18] M. J. Martinez and K. S. Udell, J. Fluid Mech. **210**, 565 (1990).

[19] S. Kuriakose and P. Dimitrakopoulos, Phys. Rev. E **84**, 011906 (2011).

[20] C. Rorai, A. Touchard, L. Zhu, and L. Brandt, Eur. Phys. J. E **38**, 49 (2015).

[21] T. Shen and F. Vernerey, Comput. Mech. **60**, 143 (2017).

[22] T. G. Fai, R. Kusters, J. Harting, C. H. Rycroft, and L. Mahadevan, Phys. Rev. Fluids **2**, 113601 (2017).

[23] F. F. Nazzal and M. R. Wiesner, Water Environ. Res. **68**, 1187 (1996).

[24] F. Y. Leong, Q. Li, C. T. Lim, and K.-H. Chiam, Biomech. Model. Mechanobiol. **10**, 755 (2011).

[25] M. Farsad and F. J. Vernerey, Int. J. Numer. Methods Eng. **92**, 238 (2012).

[26] Z. Zhang, J. Xu, B. Hong, and X. Chen, Lab Chip **14**, 2576 (2014).

[27] Z. Zhang, X. Chen, and J. Xu, Biomicrofluidics **9**, 024108 (2015).

[28] Z. Zhang, C. Drapaca, X. Chen, and J. Xu, Phys. Fluids **29**, 072102 (2017).

[29] E. Benet and F. J. Vernerey, Phys. Rev. E **94**, 062613 (2016).

[30] A. G. Yiotis, L. Talon, and D. Salin, Phys. Rev. E **87**, 033001 (2013).

[31] L. C. Foucard and F. J. Vernerey, Int. J. Numer. Methods Eng. **102**, 79 (2015).

[32] L. C. Foucard, J. Pellegrino, and F. J. Vernerey, Comput. Model. Eng. Sci. **98**, 101 (2014).

[33] D. Mollison, J. R. Stat. Soc. Ser. B **39**, 283 (1977).

[34] E. Albano, J. Phys. A **27**, L881 (1994).

[35] D. Ben-Avraham, Chemometrics Intell. Lab. Syst. **10**, 117 (1991).

[36] J. J. Telega and W. R. Bielski, Comput. Geotech. **30**, 271 (2003).

[37] G. N. Constantinides and A. C. Payatakes, AIChE J. **42**, 369 (1996).

[38] G. Wagner, A. Birovljev, P. Meakin, J. Feder, and T. Jossang, Phys. Rev. E **55**, 7015 (1997).

[39] J. Schmittbuhl, A. Hansen, H. Auradou, and K. J. Måløy, Phys. Rev. E **61**, 3985 (2000).

[40] C. Kaiser, Transp. Porous Media **26**, 133 (1997).

[41] M. Thullner, Ecol. Eng. **36**, 176 (2010).

[42] N. Tufenkji, Adv. Water Resour. **30**, 1455 (2007).

[43] E. Benet, A. Badran, J. Pellegrino, and F. Vernerey, J. Membr. Sci. **535**, 10 (2017).

[44] M. Prakash and N. Gershenfeld, Science **315**, 832 (2007).

[45] N. Champagne, R. Vasseur, A. Montourcy, and D. Bartolo, Phys. Rev. Lett. **105**, 044502 (2010).

[46] R. M. Hochmuth, J. Biomech. **33**, 15 (2000).

[47] S. Teh, R. Lin, L.-H. Hung, and A. P. Lee, Lab Chip **8**, 198 (2008).

[48] E. N. Tummons, V. V. Tarabara, J. W. Chew, and A. G. Fane, J. Membr. Sci. **500**, 211 (2015).

[49] M. M. Dias and A. C. Payatakes, J. Fluid Mech. **164**, 305 (1986).

[50] M. M. Dias and A. C. Payatakes, J. Fluid Mech. **164**, 337 (1986).

[51] S. Mochizuki and A. L. Zydney, J. Membr. Sci. **82**, 211 (1993).

[52] A. C. Payatakes, K. M. Ng, and R. W. Flumerfelt, AIChE J. **26**, 430 (1980).

[53] H. Hinrichsen, Adv. Phys. **49**, 815 (2000).

[54] J. W. Essam, A. J. Guttmann, and K. De'Bell, J. Phys. A **21**, 3815 (1988).

[55] J. Wang, Z. Zhou, Q. Liu, T. M. Garoni, and Y. Deng, Phys. Rev. E **88**, 042102 (2013).

[56] J. W. Essam, K. De'Bell, J. Adler, and F. M. Bhatti, Phys. Rev. B **33**, 1982 (1986).

[57] D. Stauffer and A. Aharony, arXiv:0712.0689.

[58] C. Kaiser and L. Turban, J. Phys. A **27**, L579 (1994).

[59] W. Engl, M. Roche, A. Colin, P. Panizza, and A. Ajdari, Phys. Rev. Lett. **95**, 208304 (2005).

[60] F. Jousse, R. Farr, D. R. Link, M. J. Fuerstman, and P. Garstecki, Phys. Rev. E **74**, 036311 (2006).

[61] F. J. Vernerey, Int. J. Solids Struct. **48**, 3129 (2011).

[62] F. J. Vernerey, Transp. Porous Media **93**, 815 (2012).

[63] F. J. Vernerey, R. Long, and R. Brighenti, J. Mech. Phys. Solids **107**, 1 (2017).

[64] F. Vernerey and T. Shen, J. R. Soc., Interface **14**, 20170242 (2017).

[65] U. Akalp, S. J. Bryant, and F. J. Vernerey, Soft Matter **12**, 7505 (2016).

[66] S. J. Bryant and F. J. Vernerey, Adv. Healthcare Mater. **7**, 1700605 (2018).

[67] S. L. Sridhar, M. C. Schneider, S. Chu, G. De Roucy, S. J. Bryant, and F. J. Vernerey, Soft Matter **13**, 4801 (2017).